Observation-Based Longwave Cloud Radiative Kernels Derived from the A-Train

QING YUE, BRIAN H. KAHN, ERIC J. FETZER, MATHIAS SCHREIER, AND SUN WONG

Jet Propulsion Laboratory, California Institute of Technology, Pasadena, California

XIUHONG CHEN AND XIANGLEI HUANG

Department of Atmospheric, Oceanic, and Space Sciences, University of Michigan, Ann Arbor, Michigan

(Manuscript received 30 March 2015, in final form 6 January 2016)

ABSTRACT

The authors present a new method to derive both the broadband and spectral longwave observation-based cloud radiative kernels (CRKs) using cloud radiative forcing (CRF) and cloud fraction (CF) for different cloud types using multisensor A-Train observations and MERRA data collocated on the pixel scale. Both observation-based CRKs and model-based CRKs derived from the Fu–Liou radiative transfer model are shown. Good agreement between observation- and model-derived CRKs is found for optically thick clouds. For optically thin clouds, the observation-based CRKs show a larger radiative sensitivity at TOA to cloud-cover change than model-derived CRKs. Four types of possible uncertainties in the observed CRKs are investigated: 1) uncertainties in Moderate Resolution Imaging Spectroradiometer cloud properties, 2) the contributions of clear-sky changes to the CRF, 3) the assumptions regarding clear-sky thresholds in the observations, and 4) the assumption of a single-layer cloud. The observation-based CRKs show the TOA radiative sensitivity of cloud types to unit cloud fraction change as observed by the A-Train. Therefore, a combination of observation-based CRKs with cloud changes observed by these instruments over time will provide an estimate of the short-term cloud feedback by maintaining consistency between CRKs and cloud responses to climate variability.

1. Introduction

Climate model simulations exhibit a wide range of climate variability and future climate projections in response to increased greenhouse gases (e.g., Bony et al. 2006; Stephens 2005). Cloud feedback has been identified as a major source of this intermodel spread (e.g., Dufresne and Bony 2008; Vial et al. 2013). While the past 10 years of satellite cloud observations have not detected a trend for global cloud amount, opposite trends have been detected for high and low cloud (Marchand 2013). Different cloud types have very distinct longwave and shortwave radiative effects and introduce a widely varying intermodel spread in cloud feedbacks (Hartmann et al. 1992; Webb et al. 2006; Williams and Tselioudis 2007; Williams and Webb 2009; Zelinka et al. 2012). Moreover, many studies have shown remote sensing instruments often have strengths and limitations related to different cloud types in the instrument's field of view (FOV) (e.g., Yue et al. 2013; Pincus et al. 2012). Therefore, active research efforts have been dedicated to analyzing and understanding the cloud feedbacks and their relationships with different cloud types from both observations and climate models (IPCC 2013).

Typically, the cloud feedback is quantified as the change in the cloud radiative forcing (CRF) per unit change in the global mean surface air temperature (in $\mathrm{W\,m^{-2}\,K^{-1}}$) after accounting for and removing the effect of clear-sky change on the total CRF change (cloud masking effect; Soden et al. 2004, 2008; Shell et al. 2008), where CRF is defined as the difference between the clear- and all-sky TOA fluxes (in $\mathrm{W\,m^{-2}}$; e.g., Charlock and Ramanathan 1985). Previous studies have inferred cloud feedback from satellite observations using a correlation methodology (Gregory et al. 2002). Dessler (2010) and Dessler and Loeb (2013) estimated the short-term cloud feedback by correlating the change of TOA CRF due to cloud change ΔR_{CRF} with the surface temperature change ΔT_s arising from El Niño–Southern Oscillation (ENSO) variations. They used monthly

Corresponding author address: Dr. Qing Yue, Jet Propulsion Laboratory, 4800 Oak Grove Drive, Mail Stop 233-302C, Pasadena, CA 91109.
E-mail: qing.yue@jpl.nasa.gov

DOI: 10.1175/JCLI-D-15-0257.1

averages of satellite and reanalysis TOA all-sky fluxes and reanalysis clear-sky fluxes and meteorological fields. A large spread and uncertainty were obtained with respect to the global mean short-term cloud feedbacks, primarily due to two factors: 1) large uncertainties of measurements and different reanalysis datasets and 2) compensation of signals from different cloud types, geographical regions, and altitudes where clouds change with climate.

The radiative kernel method (Held and Soden 2000; Soden and Held 2006) has been extensively used to calculate feedbacks. One of its advantages is that the kernels, developed from base climate states using relatively small amounts of data [e.g., Soden et al. (2008) suggest that 1 year of simulation is sufficient for computing the kernels], can be applied in both observational and model studies. The radiative kernel method separates feedbacks into two factors: the radiative kernel and the climate response pattern. Scaling the response with the appropriate radiative kernels then yields the climate feedback parameter. As stated in Soden and Held (2006), because of the strong nonlinearities in the calculation of the radiative adjoint arising from the vertical structure of cloud, cloud radiative kernels (CRKs) were not computed by perturbing cloud property vertical profiles in radiative transfer calculations. These noncloud radiative kernels have been used to adjust the total CRF change observed by satellite to reflect changes solely due to cloud properties to obtain cloud feedback from observations (Dessler 2010), although the individual cloud regimes are not revealed using this method.

Alternatively, using a cloud classification approach, Zelinka et al. (2012) introduced a method to quantify the cloud feedbacks as a joint function of cloud-top pressure (CTP) and cloud optical depth τ based on cloud fraction changes from output of the International Satellite Cloud Climatology Project (ISCCP) cloud simulator (Klein and Jakob 1999; Webb et al. 2001). A set of CRKs was calculated using the Fu and Liou (1992) radiative transfer scheme with model-mean atmospheric states and a series of assumptions regarding a single-layer cloud and surface radiative properties. Zhou et al. (2013) calculated CRKs following this method but replaced the model temperature and moisture profiles with the monthly mean fields from the European Centre for Medium-Range Weather Forecasts (ECMWF) interim reanalysis (ERA-Interim) over the NASA Earth Observing System (EOS) *Terra* satellite period. These previously developed CRKs are based on cloudy-sky radiative transfer model calculations with synthetic cloud properties, which show the radiative sensitivity of cloud at the TOA with the input CTP as effective radiative cloud top. To reduce the errors in the feedback calculation caused by dependence of these CRKs on particular radiative transfer models and thus the errors in reproducing TOA radiative fluxes, Sanderson and Shell (2012) further developed a statistical approach to optimize the CRKs developed by Zelinka et al. (2012) for applications in specific global circulation models. For simplicity, we refer to these aforementioned CRKs as model-based CRKs.

By combining the model-based CRKs and cloud fraction changes for different CTP–τ bins as observed by *Terra* Moderate Resolution Imaging Spectroradiometer (MODIS) instrument, Zhou et al. (2013) examined the short-term cloud feedback by cloud type defined on a joint CTP–τ histogram. However, directly applying the model-based CRKs to observed cloud fraction changes introduces a basic inconsistency between the kernels and the climate response term. The clouds that produce the TOA radiative sensitivity are based on radiative transfer modeling of synthetic single-layer cloud at a layer specified by CTP, as shown by model-based CRKs. These radiative sensitivities may not correctly represent or correspond with the clouds observed/retrieved by satellite instruments that produce the climate change response of cloud. This inconsistency introduces errors when applying model-based CRKs to MODIS cloud observations as pointed out in Zhou et al. (2013). Two potential issues contribute to the inconsistency. One is that satellite observations such as MODIS may misclassify cloud types so that the cloud fraction change (the climate response of cloud) does not correspond with the model-based CRKs. The other is that depending on instruments and retrieval algorithms, the observed CTP may not be consistent with TOA radiative fluxes. For instance, in the MODIS collection 5 (C5) data product, the low-cloud CTP is retrieved using an infrared window method, while for middle and high cloud, the CO_2-slicing method (Chahine 1974) is used and tends to give a CTP higher in altitude than the radiative cloud top. For active sensors such as *CloudSat*, the CTP is a more direct measure of the geometric cloud top, which is different from the effective radiative cloud top that is used in the previous model-based CRKs.

The A-Train constellation of satellites (Stephens et al. 2002) provides over a decade of continuous observations of spatially and temporally coincident atmospheric state, radiative fluxes, and cloud properties, providing an ideal toolkit for quantifying cloud radiative sensitivity and its relationship with cloud type and atmospheric thermodynamic state. Therefore, it is feasible to develop new methods and tools using the A-Train observations for cloud feedback studies. Moreover, the Atmospheric Infrared Sounder (AIRS) spectral outgoing longwave radiation (OLR) dataset (Huang et al. 2008, 2010, 2013) provides the spectral dimension of OLR and longwave

CRF, which can help better reveal the connection between the longwave band-by-band fluxes and properties of cloud and atmospheric states (Huang et al. 2014a). Huang et al. (2014b) derived spectral noncloud radiative kernels and applied these kernels to models from phases 3 and 5 of the Coupled Model Intercomparison Project (CMIP3 and CMIP5). They found that the climate feedbacks in different spectral windows show distinct regional distributions and different ranges of intermodel spread than their broadband counterpart. They also noticed that the good agreement among some models on the broadband feedbacks is the result of compensation of large biases in different spectral regions. The spectral cloud feedback, especially in the longwave, has not yet been directly examined in observations and additional spectral information may be revealed.

In this study, we outline a new approach to derive observation-based CRKs from satellite observations of cloud and TOA radiative fluxes from simultaneous collocated observations at the instrument pixel scale obtained by AIRS (Aumann et al. 2003) and Advanced Microwave Sounding Unit (AMSU; Lambrigtsen and Lee 2003), MODIS (Barnes et al. 1998), and Clouds and the Earth's Radiant Energy System (CERES; Wielicki et al. 1996). All of these instruments are onboard the EOS *Aqua* satellite. A set of spectral longwave CRKs is also developed utilizing the AIRS spectral OLR dataset. Although the CRKs derived here are based on the measurements from *Aqua*, the method proposed here can be generalized to other satellite platforms and different cloud classification methods. For comparison purposes, we also derive a set of model-based CRKs using collocated NASA's Modern-Era Retrospective Analysis for Research and Applications (MERRA) data (Suarez et al. 2008; Rienecker et al. 2011) and MODIS cloud properties as input to Fu and Liou (1992) model calculations of OLR. Since the observation-based CRKs are empirically derived from satellite observations, it quantifies the TOA radiative sensitivity of different cloud types to cloud fraction changes as observed by the same set of instruments and hence will maintain the consistency between kernel and climate response terms of clouds when estimating cloud feedbacks from observation.

Directly estimating the long-term cloud feedback from A-Train satellite observations is not yet possible because of the short data record. Moreover, inherent limitations of the instruments (e.g., sensitivity, resolution, and sampling) and the retrieval algorithms (including forward radiative transfer models used in the retrieval and inverse method) may enhance uncertainties in the derived geophysical observations. We present a detailed uncertainty study on the observation-based longwave CRKs, which can be applied to estimate short-term cloud feedback from satellite observations. Shortwave CRKs and cloud feedback estimates from satellite observations will be reported elsewhere.

This paper is organized as follows. The data and methodology are outlined in section 2. Results and a discussion on uncertainties are presented in section 3, and a summary of the results is presented in section 4.

2. Data and methodology

a. Data

We construct a monthly global gridded (2.5° × 2.5°) climatological dataset of atmospheric temperature and moisture, cloud properties, and TOA radiative fluxes that are stratified by cloud type. This dataset is based on collocated nearest-neighbor multisensor satellite measurements and instantaneous MERRA atmospheric and surface states (Rienecker et al. 2011) at the pixel scale of AIRS–AMSU (~45 km).

The EOS *Aqua* satellite was the first in the A-Train satellite constellation. *Aqua* has a near-polar inclination (98°) and low-Earth orbit (705 km) with equatorial crossing times of 0130 (descending) and 1330 (ascending) LT. Launched on 4 May 2002, *Aqua* carries six Earth-observing instruments collecting simultaneous observations of radiation, cloud and aerosols, precipitation, and atmospheric state (Parkinson 2003). Therefore, the *Aqua* data are uniquely suited to investigate cloud radiative effects and TOA radiative sensitivity to various atmospheric and cloud states. The sensitivity of TOA radiative fluxes to different perturbations of climate variables in the Earth system is closely related to radiative feedbacks and climate sensitivity.

We use data from AIRS–AMSU, MODIS, and CERES on *Aqua*. All of the level 2 (L2) swath data are collocated at the native retrieved pixel scale to ensure close correspondence among radiation, cloud, and atmospheric states, an essential prerequisite of and unique contribution to this study. Atmospheric states, cloud, and radiation are tightly coupled and cloud processes operate on very short time scales, so increasing spatial and temporal averaging will average out the signal of this coupling. MERRA data are collocated to the *Aqua* swath data using a nearest-neighbor approach to provide a comprehensive set of surface and atmospheric properties.

The TOA radiation fluxes are obtained from the collocated AIRS and CERES data using the algorithms developed and validated in Huang et al. (2008, 2010) over the tropical oceans and Chen et al. (2013) and Huang et al. (2014a) over the entire globe. These data provide a global dataset of spectrally resolved TOA OLR, broadband OLR, and upward shortwave flux. The broadband fluxes are obtained from the CERES L2 footprint data

product, the single satellite footprint (SSF) TOA–surface fluxes and clouds edition 3A (Loeb et al. 2005), which is collocated with AIRS–AMSU FOV using the method in Huang et al. (2008). The spectrally resolved OLR covers a range of 10–2000 cm^{-1} at a resolution of 5 cm^{-1}. It is converted from the AIRS geo-collocated and calibrated infrared radiances using the spectrally dependent angular distribution models developed by Huang et al. (2008, 2010).

Cloud types are specified by histograms partitioned by MODIS CTP and τ. We follow the tradition of ISCCP cloud histograms (Rossow and Schiffer 1999) used in Zelinka et al. (2012) and define 49 cloud types partitioned by seven CTP bins (edges at 50, 180, 310, 440, 560, 680, 800, and 1000 hPa) and seven τ bins (edges at 0, 0.3, 1.3, 3.6, 9.4, 23, 60, and >60), with three definitions of clear sky that use different thresholds of cloud amount that will be discussed further below.

We use three different sets of cloud observations: the effective cloud fraction (ECF) retrieved by AIRS (Kahn et al. 2014), the standard MODIS cloud products from the MODIS atmosphere science team (MAST-MODIS; Platnick et al. 2003), and the CERES team MODIS cloud products (CERES-MODIS; Minnis et al. 2011a). The ECF retrieved by AIRS is a radiatively effective cloud fraction, equivalent to the product of cloud area fraction and cloud infrared emissivity. Since AIRS is more sensitive to thin cirrus, we use AIRS ECF to ''screen out'' additional thin cirrus that the operational MODIS algorithm may miss (Yue et al. 2007; Kahn et al. 2014).

For the MAST-MODIS cloud products, we use the C5 L2 cloud properties (MYD06_L2). The CERES-MODIS cloud products are from the CERES SSF TOA–surface fluxes and clouds edition 3A. Both sets of MODIS cloud products provide a cloud mask, effective radius r_e, τ, cloud-top temperature (CTT), and CTP. However, the two MODIS datasets are based on two different retrieval algorithms and use two different subsets of MODIS channels. A detailed description of the differences is found in Minnis et al. (2011a,b). As shown below, the impact of the different MODIS cloud retrieval algorithms is smaller on the observation-based longwave CRK than on CRF and cloud fraction (CF), especially for optically thin clouds.

The MODIS cloud property measurements are matched to radiation and atmospheric parameters obtained from collocated AIRS–AMSU–CERES–MERRA data using the collocation method developed by Schreier et al. (2010). Approximately 200 1-km MODIS pixels are collocated within a given AIRS FOV; only those within 45° of nadir are used to avoid distortion and rotation of the FOV associated with higher scan angles. As a result, 11.25% of MODIS data are excluded. Averaged MODIS cloud fraction is calculated at the AIRS–AMSU resolution by averaging all MODIS pixels within the AIRS–AMSU FOV. Cloud r_e, τ, CTT, and CTP are averaged only over the cloudy MODIS pixels identified as confident or probably cloud according to the MODIS 1-km cloud mask. The two MODIS cloud retrieval datasets are used as a proxy to estimate how sensitive the observation-based CRKs are to uncertainties in observed MODIS cloud parameters. They are also useful to highlight the importance of consistency between CRKs and cloud fraction changes in estimating short-term cloud feedback from observations.

Since τ is used to classify cloud type, only sunlit portions of the globe that are along the A-Train orbit are sampled, including daytime and polar latitude summer at the A-Train overpass time. This sampling bias impact on observation-based CRKs has not been quantified yet, although the model-based CRKs derived in our study and in earlier studies do account for solar zenith angle changes through the 24-h day. The daytime-only sampling impact was previously quantified by Zelinka et al. (2012) and concluded that there is little discernible impact on the longwave feedbacks. Moreover, the use of daytime-only MODIS cloud mask data avoids a potential inconsistency that arises from different methods used for nighttime cloud detection (Platnick et al. 2003).

Different from the MAST-MODIS cloud retrieval algorithm, the CERES-MODIS cloud properties are reported up to two cloud layers for each pixel at the nadir resolution of 20 km (Minnis et al. 2011a). The column-mean cloud fraction is calculated as the summation over two cloud layers, and the mean CTP and τ are calculated as the average of values on different layers weighted by layer CF.

Clear sky is obtained from a subset of pixels that have cloud fraction less than a specified threshold. In this study, three different clear types are defined: Clear-1 (AIRS ECF < 0.05), Clear-2 (AIRS ECF < 0.01), and Clear-3 (MODIS CF < 0.05). Unless specified, the results are based on the clear-sky definition of Clear-2, the most stringent among the three thresholds.

The pixel-scale, temporally and spatially collocated, multisensor satellite and MERRA data are then gridded to 2.5° × 2.5° resolution to construct a monthly mean global dataset. For each grid box, AIRS–AMSU pixel-scale observations are collected for each month and binned by cloud type using 7 × 7 CTP–τ cloud histograms and three clear thresholds described above. As a result, monthly means of AIRS spectral OLR, CERES TOA fluxes, cloud properties, and atmospheric states are reported by cloud type at each grid box.

b. *Cloud radiative forcing*

The effect of clouds on Earth's TOA radiation balance is measured as the difference between clear-sky

and all-sky TOA radiative fluxes. This difference is defined as the TOA CRF. In a partly cloudy region consisting of an overcast region with fractional coverage C and a clear-sky region with fractional coverage $1 - C$, the all-sky TOA flux is expressed as follows:

$$F_{\text{all\_sky}} = (1 - C)F_{\text{clr}} + CF_{\text{ovc}}, \quad (1)$$

where F_{clr} and F_{ovc} are the fluxes over the clear and overcast portion of a region or grid box, respectively. Then the CRF is written as follows:

$$\text{CRF} = F_{\text{clr}} - F_{\text{all\_sky}} = C(F_{\text{clr}} - F_{\text{ovc}}). \quad (2)$$

If the term $\text{CRF}_{\text{ovc}} = (F_{\text{clr}} - F_{\text{ovc}})$ is defined to be the CRF if such cloud would have 100% coverage (overcast), then the following relationship results:

$$\text{CRF}_{\text{ovc}} = \text{CRF}/C. \quad (3)$$

c. CRK method

The CRK method (Zelinka et al. 2012) was proposed to directly determine the cloud radiative feedback for various cloud types using the concept of a radiative kernel. This technique makes use of histograms of TOA radiative flux sensitivities to cloud fraction changes that are partitioned by the ISCCP cloud-type convention.

The radiative flux sensitivity is defined as the CRK, which is calculated as the perturbation of TOA CRF resulting from a unit change in cloud fraction C for each cloud type as follows:

$$\text{CRK} = \partial\text{CRF}/\partial C. \quad (4)$$

As discussed in the introduction, two previous sets of model-based CRKs have been developed (Zelinka et al. 2012; Zhou et al. 2013). Both are based on radiative transfer calculations using the Fu and Liou (1992) model assuming a synthetic single-layer cloud with 100% areal coverage. The atmospheric temperature and water vapor profiles required in the radiative transfer calculation are the climatological zonal and monthly mean profiles averaged across six CMIP3 models (Zelinka et al. 2012) or ERA-Interim (Zhou et al. 2013). A single-layer homogeneous cloud is inserted to the level closest to the specified CTP with 100% cloud cover (overcast) and fixed r_e (10 and 30 μm for liquid and ice cloud, respectively). The CTT is used to partition the cloud phase; ice (liquid) phase is used for clouds with tops colder (warmer) than 263 K. Radiative transfer calculations are performed using the cloud properties (r_e and pairs of CTP and τ) for each of the four corners of a cloud histogram bin and are averaged to determine the TOA fluxes for that bin. Surface emissivity is assumed to be 0.99 everywhere. Corresponding clear-sky fluxes are calculated by setting the cloud amount to zero while retaining identical atmospheric states. The CRF is calculated for each cloud histogram bin by differencing clear- and overcast-sky fluxes. Dividing the overcast-sky CRF matrix by 100 expresses the change of TOA flux resulting from a unit change of cloud cover that is the CRK (in units of $\text{W m}^{-2}\ \%^{-1}$).

d. Observation-based CRK

We derive a CRK matrix as a function of cloud type by combining flux and cloud observations. Following Eq. (2), the CRF at each 2.5° × 2.5° grid box for each cloud type is calculated as the difference between monthly means of cloudy and clear pixels only if cloudy observations of a given cloud type and clear pixels are both available in that grid box. The differences in atmospheric temperature and moisture structure between clear and cloudy conditions contribute to a radiative flux difference at TOA that is not directly due to the cloud properties (Zhang et al. 1994b). This radiative effect is included in the CRF derived from observations. While models can calculate clear-sky fluxes assuming the same atmospheric states for clear- and all-sky conditions, observations cannot directly measure this atmospheric contribution to CRF. Therefore, it should be removed from observed CRF before CRK is calculated and subsequently compared with model-based results. After removing the atmospheric contribution to CRF, the overcast-sky CRF (CRF_{ovc}) is derived by dividing all-sky CRF by C as in Eq. (3). The CRK is then obtained in the same manner as Zelinka et al. (2012) by dividing CRF_{ovc} by 100.

There are two major differences between this CRK and the previous two sets of CRKs developed in Zelinka et al. (2012) and Zhou et al. (2013). First, this CRK is empirically derived based on satellite observations and does not require additional cloudy-sky radiative transfer calculations and assumptions about cloud properties in the radiative transfer calculation; however, this kernel is dependent on the satellite retrieval algorithms used and the accuracy of atmospheric states from the MERRA data (see discussion below). Second, since the native satellite spatial resolution is not fine enough to identify every clear patch of sky, there are regions that always appear overcast. As a result, clear and cloudy skies have different spatial coverage and sampling characteristics, which affects the observation-based CRF and CRK calculations. Therefore, the CRF and CRK are calculated for locations over which both clear and cloudy pixels are available within a short time span (one month in this study).

THE CONTRIBUTION OF THE ATMOSPHERE ON THE OBSERVATION-BASED CRF AND CRK

Since MERRA data are also collocated, the monthly mean atmospheric states and surface conditions for each cloud type (including clear sky) are obtained at each grid box from MERRA. Based on Eq. (2), CRF in a given grid box for a given cloud type is calculated as the combination of $F_{\rm clr}$ and $F_{\rm ovc}$:

$$\mathrm{CRF[observed.clear]} = C(F_{\rm clr}[\mathrm{observed.clear}] - F_{\rm ovc}),$$

and

$$\mathrm{CRF[cloud.removed]} = C(F_{\rm clr}[\mathrm{cloud.removed}] - F_{\rm ovc}).$$

Here, $F_{\rm ovc}$ is the flux from the overcast portion of the observation and is the same regardless of how $F_{\rm clr}$ is extracted: the atmosphere from the subset of clear pixels in each grid box (denoted with [observed.clear]), or atmospheric states in cloudy skies but setting cloud amount to zero in a radiative transfer calculation (denoted with [cloud.removed]). The atmosphere contribution to observation-based CRF, termed as MΔCRF to indicate its connection with the cloud masking effect (e.g., Soden et al. 2004, 2008; see discussion below), is the difference between the two CRFs:

$$\begin{aligned}\mathrm{M\Delta CRF} &= \mathrm{CRF[observed.clear]} - \mathrm{CRF[cloud.removed]}\\ &= C(F_{\rm clr}[\mathrm{observed.clear}] - F_{\rm clr}[\mathrm{cloud.removed}]).\end{aligned} \tag{5}$$

Here, MΔCRF is the cloud radiative effect contributed from atmospheric temperature and moisture profiles that are correlated with cloud type but are not directly related with the cloud radiative effects from cloud properties such as τ, r_e, and CTT/CTP. Following Dessler (2010) and Dessler and Loeb (2013), MΔCRF can be estimated using the MERRA clear-sky radiative fluxes that are calculated from setting the cloud amount to zero. Another method is to compute MΔCRF as the difference between two clear-column radiative transfer calculations using the monthly mean atmospheric data, as done in this study. We compared the two methods and small differences are found in the results. We assume that the difference of atmospheric states between clear and cloudy skies for a given cloud type does not change greatly over time if considered at the same spatial location and time of year. (Note that this assumption is made only for monthly statistics. However, in the instantaneous data, there is a large variation of this difference that is a function of location, time, cloud, etc.) Thus, MΔCRF can be quantified and therefore removed from observed total CRF through two clear-sky radiative transfer calculations. In this work, the atmospheric columns under [observed.clear] and [cloud.removed] is based on global gridded (2.5° × 2.5°) monthly mean temperature and water vapor profiles and surface properties categorized by cloud types by collocating MERRA with the L2 MODIS cloud observations. Clear-sky radiative transfer calculations of $F_{\rm clr}$[observed.clear] are used instead of CERES observed flux from clear pixels to exclude the inconsistency between observed and calculated fluxes caused by additional assumptions in radiative transfer calculations.

Zhang et al. (1994a) compared different methods that extract clear-sky fluxes and cloud radiative effects from satellite observations and model simulations. Using Earth Radiation Budget Experiment (ERBE) data, they showed that the number of clear-sky days is sensitive to the cloud amount threshold values and causes a TOA OLR difference of more than 10 W m^{-2} in regions with persistent cloud cover. Ramanathan et al. (1989) used temporally and spatially averaged clear-sky fluxes to estimate CRF from ERBE measurements based on their finding that clear-sky fluxes are more homogeneous than cloudy-sky fluxes. Using this method, the error of clear-sky fluxes depends on region and the spatial resolution of the data but is estimated to be smaller than 10 W m^{-2}. Since atmospheric temperature and moisture profiles are strongly correlated with cloud regime (e.g., Yue et al. 2013; Wong et al. 2015), we quantify MΔCRF and its contribution to CRF and CRK separately for each cloud type.

From Eqs. (4) and (5), the observation-based CRK can be calculated as follows:

$$\begin{aligned}\mathrm{CRK} &= \partial(\mathrm{CRF[observed.clear]} - \mathrm{M\Delta CRF})/\partial C\\ &= \partial\mathrm{CRF[observed.clear]}/\partial C - \partial(\mathrm{M\Delta CRF})/\partial C.\end{aligned} \tag{6}$$

For a unit change in C, $\partial\mathrm{M\Delta CRF}/\partial C$ represents the atmospheric contribution to the change of TOA radiative flux at unit change of C. This effect is related to but is different from the cloud masking effect in model climate feedback studies (e.g., Soden et al. 2004, 2008; Shell et al. 2008; Lambert et al. 2014). The cloud masking effect accounts for the effect of cloud on the radiative perturbations introduced by changes in other quantities (e.g., CO_2 and water vapor) because the clear- and cloudy-sky OLR may respond differently to the same forcing (e.g., doubling of CO_2). As defined here, MΔCRF is caused by the difference between cloudy and clear atmospheric columns in the same climate state. The overarching goal here is to remove it from the observed CRF to obtain CRF that is caused solely by

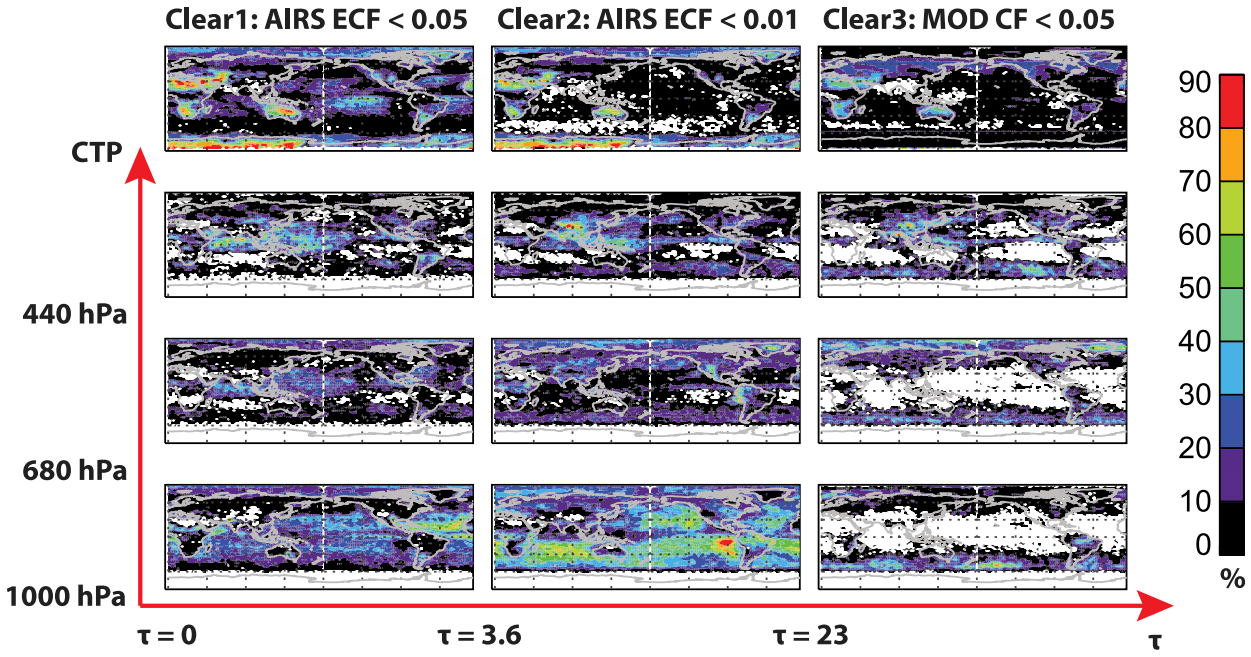

FIG. 1. (top) The global distributions of the occurrence frequencies for the three clear-sky thresholds and (middle)–(bottom) the occurrence frequencies for the 3 × 3 ISCCP-defined cloud types for July 2009. The cloud types are defined using a histogram of CTP and τ from MAST-MODIS data. The bin edges of CTP and τ are indicated along the red axes. Color bar shows percentage (%).

cloud properties from which the observation-based CRK is derived.

e. *Model-based CRKs from collocated datasets*

We also derive a model-based CRK following the method of Zelinka et al. (2012) and Zhou et al. (2013) using the Fu–Liou model code with the same setup as in these previous studies. There are two exceptions: 1) we use MERRA atmospheric states and surface properties by cloud type, and 2) we use gridded monthly mean values of MODIS cloud properties, including τ, r_e, CTP, and CTT, for each cloud type. Additionally, two sets of radiative transfer calculations are performed to quantify the impact of cloud vertical structure on the magnitude of CRKs. The first assumes a single-layer cloud in the Fu–Liou code with the MODIS cloud properties. The second assumes that τ is vertically redistributed by using the monthly average vertical profiles of τ for each cloud type from the *CloudSat* level 2b cloud optical depth (2B-TAU) data during July 2009.

3. Results

a. *Global distribution of cloud types*

Figure 1 shows global distributions of the occurrence frequency of different cloud types gridded at 2.5° × 2.5° resolution from collocated July 2009 MAST-MODIS data. For simplicity, rather than show a 7 × 7 cloud histogram, the results are summarized in Fig. 1 as a 3 × 3 histogram with CTP partitioned at 440, 680, and 1000 hPa and τ partitioned at 3.6, 23, and >23. White indicates grid boxes that do not contain valid observations (counts ≤2). The three clear-sky distributions (Fig. 1, top) have similar spatial extents with maxima over dry continental regions such as central Australia and the Sahara Desert and minima over the southern midlatitude oceans, the subtropical stratocumulus regimes, and Southeast Asia during the summer monsoon. The mean global frequencies of the three clear-sky distributions are 21.67% (Clear-1), 12.92% (Clear-2), and 16.63% (Clear-3). The Clear-1 criterion includes some broken trade cumulus cloud occurrences over the subtropical ocean designated as ''clear.'' Since only the sunlit portion of the orbit is used, the high-latitude Southern Hemisphere is not included. Henceforth, the focus is between 65°N and 65°S using the Clear-2 criterion to obtain the clear-sky fluxes. The spatial patterns for different cloud types in Fig. 1 are consistent with previous work. A noteworthy point to take from Fig. 1 is that observations of cloudy and clear skies may not be simultaneously available at a few locations for this monthly dataset. As discussed earlier, to quantify the dependence of cloud radiative effects by cloud type, both cloudy and clear-sky samples must be present in the same grid box.

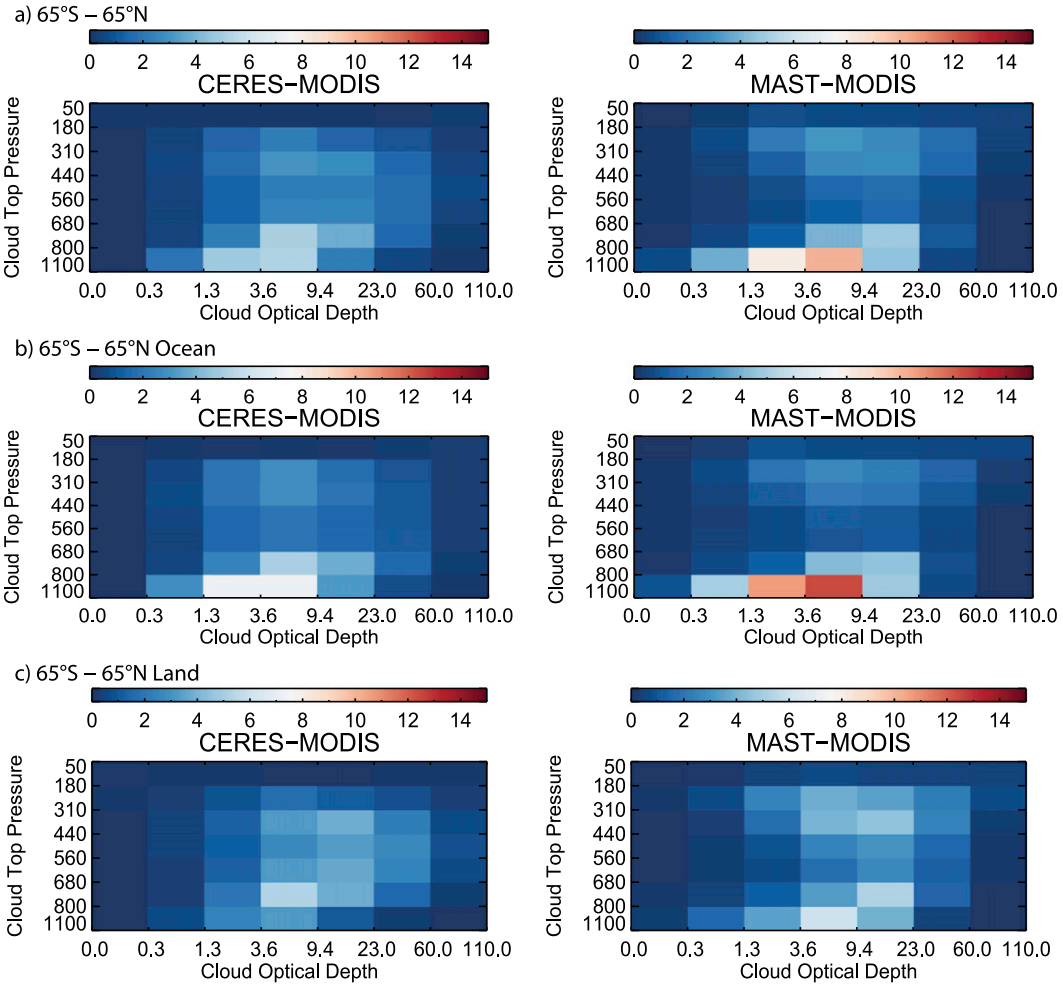

FIG. 2. The occurrence frequency for different cloud types during July 2009: (a) 65°N–65°S, (b) 65°N–65°S over ocean, and (c) 65°N–65°S over land based on (left) the CERES-MODIS cloud data collocated to the AIRS–AMSU FOV and (right) the MAST-MODIS cloud data. Color bar shows percentage (%).

Figure 2 shows the occurrence frequency organized by cloud type using the two different MODIS cloud retrievals. When combining land and ocean, both MODIS retrievals show peak occurrence frequencies for low-level clouds with τ between 3.6 and 9.4 and a secondary peak for high cloud. However, CERES-MODIS shows more frequent midlevel clouds than MAST-MODIS. When separating land and ocean, both MODIS datasets suggest more midlevel clouds over land than ocean. While CERES-MODIS shows the highest peak frequency in the same τ bin but at smaller CTP when comparing land and ocean, the peak frequency for MAST-MODIS remains at the large CTP (low cloud) but moves to a larger τ bin. This highlights an important difference between the two MODIS algorithms and that the relative sample size to the CRKs will depend on cloud type. The sample size for MAST-MODIS is between 10^3 and 10^4 for most cloud types with <100 samples for high clouds (CTP $<$ 180 hPa) with $\tau < 0.3$ and the optically thick clouds ($\tau > 60$) with CTP $>$ 560 hPa. For CERES-MODIS data, cloud types with CTP $>$ 180 hPa and $\tau < 0.3$ have sample sizes <100.

While the underdetection of clouds with $\tau < 0.4$ by the C5 MAST-MODIS algorithm is well known (Holz et al. 2008; Ackerman et al. 2008), different clear-sky thresholds cannot eliminate all of the small cloud fraction and/or optically thin cloud. Thus, caution must be taken when interpreting results for $\tau < 0.4$.

Figure 3 shows the different types of cloud fractions sorted by cloud type. The ECF and CF have a similar dependence across cloud types, increasing for higher and optically thicker clouds. However, CERES-MODIS cloud fractions for optically thin clouds are much smaller than MAST-MODIS. This results from an aspect of the MAST-MODIS C5 algorithm that filters retrievals of τ and r_e in partly cloudy pixels. For the

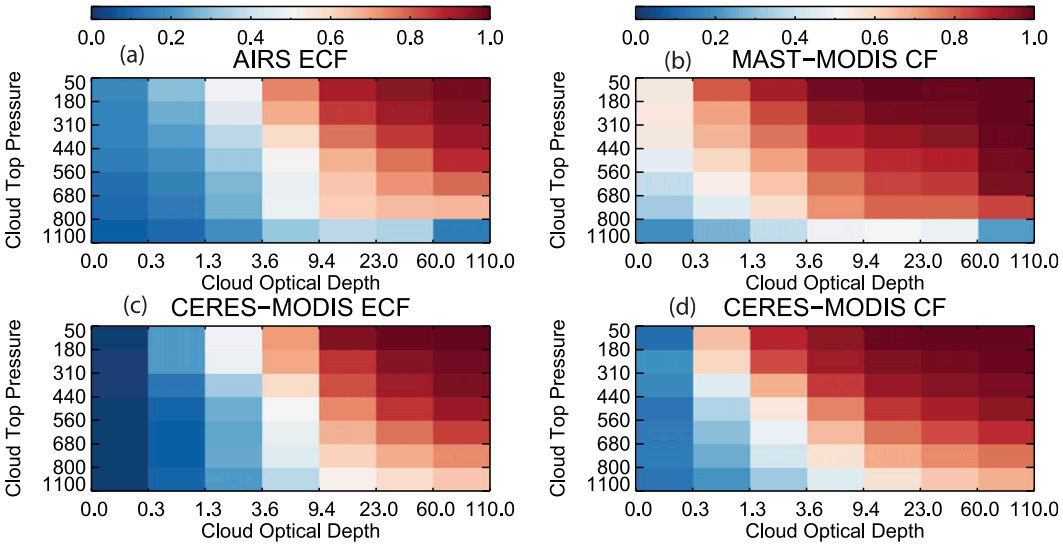

FIG. 3. ECF retrieved from (a) AIRS and (c) CERES and CF from (b) MAST-MODIS and (d) CERES-MODIS cloud data.

lowest-level cloud with large τ, CERES-MODIS CF is larger than MAST-MODIS CF. This is a result of the MAST-MODIS C5 algorithm placing clouds too high when a temperature inversion occurs, redistributing low clouds at higher altitude (Holz et al. 2008). These effects are also reflected in values of ECF (e.g., Nasiri et al. 2011). In the remainder of the paper, the cloud properties retrieved by MAST-MODIS and CERES-MODIS will be used to place approximate uncertainty bounds on the CRKs. For detailed comparison on the two MODIS-cloud retrieval algorithms (see Minnis et al. 2011a,b).

b. *Longwave CRF and MΔCRF by cloud type*

The MΔCRF that is calculated from Eq. (5) accounts for the TOA radiative effect due to different atmospheric states between clear and cloudy skies. The global mean value of MΔCRF is about 2.84 W m^{-2}, with values over land (4.55 W m^{-2}) more than twice of that over ocean (2.02 W m^{-2}). Figure 4 shows MΔCRF organized by cloud type over both land and ocean between 65°N and 65°S together with the differences of surface temperature (ΔT_{SFC}) and column water vapor (ΔCWV) calculated as the differences between clear- and cloudy-sky mean fields. Oceanic ΔT_{SFC} is negligible compared to land. However, the ΔCWV varies greatly with cloud type over both ocean and land. Deep convective clouds with correspondingly small CTP and large τ have higher CWV than clear sky in the same location. The magnitude of MΔCRF is also determined by cloud fraction [Eq. (5)]. Note that for high and thin cirrus cloud, the clear atmospheric CWV can be slightly larger than the cloudy atmosphere.

Figure 5 shows the cloud-type CRF after removing MΔCRF. The OLR (not shown) and longwave CRF distributions as functions of cloud type are very consistent among the three different datasets (MAST-MODIS and CERES fluxes, CERES-MODIS and CERES fluxes, and the Fu–Liou model calculation) although with significant discrepancies in the CRF magnitudes (see Fig. 8). The largest differences are for optically thin clouds where the uncertainties in clear-sky discrimination and MODIS cloud properties are largest.

The contribution of MΔCRF to the total OLR is 10% or less and is largest for optically thick high clouds (Fig. 4a, top right). However, the contribution of MΔCRF to total CRF is much different as shown in Fig. 5d. For thick high clouds, MΔCRF still accounts for about 10% of total CRF; however, for low and midlevel clouds, its contribution is as large as 28%. While existing noncloud radiative kernels (e.g., Soden et al. 2008; Shell et al. 2008) are derived based on perturbations of OLR, the CRK is derived from changes in TOA CRF and thus is more sensitive to the contribution of MΔCRF, which will be shown below.

c. *Longwave CRK*

Using Eq. (4), we calculate the observation-based CRKs from CRF (Fig. 5) and CF (Fig. 3) as shown in Figs. 6a and 6b. They are derived empirically from observations without additional cloudy-sky radiative transfer calculations and assumptions regarding cloud properties. The two MODIS cloud retrievals are quite different with respect to CF distributions and CRF values (see Fig. 8), and for optically thin cloud, the difference can

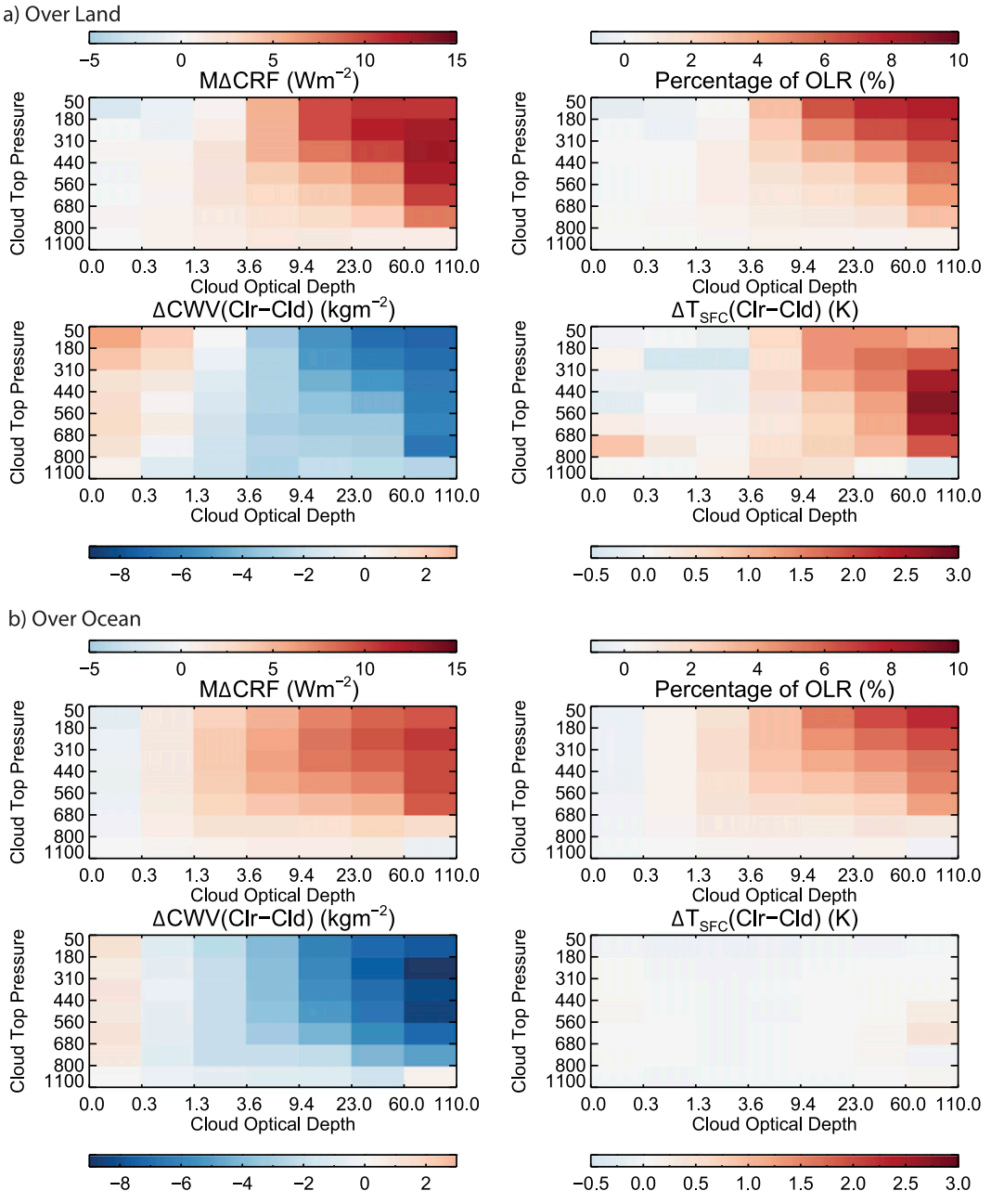

FIG. 4. MΔCRF by cloud type that is caused by the difference in clear and cloudy atmosphere states for 65°N–65°S over (a) land and (b) ocean. Also shown are the percentages of the MΔCRF in OLR and the ΔT_{SFC} and ΔCWV by cloud type between clear and cloudy atmospheric columns.

be more than 100%. However, the difference on the CRK is only from −0.4 to +0.1 W m^{-2} %$^{-1}$. The relative magnitude is much smaller for cloud types with $\tau < 3.6$ because of the compensation between cloud retrieval algorithm effects on CF and on CRF. For low clouds with $\tau > 9.6$, the relative difference reaches 30%–45%.

Also shown in Fig. 6c are the longwave CRKs calculated using the Fu–Liou model with MAST-MODIS cloud properties and MERRA thermodynamic profiles and surface properties. We also show the July CRKs from the study in Zhou et al. (2013) that are based on means derived from ERA-Interim over the EOS *Terra* satellite period and assumed cloud properties following the method in Zelinka et al. (2012). A notable difference between the results shown in Fig. 6c and Fig. 6d is related to the data sampling. Figure 6c uses collocated MERRA and AIRS–MODIS cloud observations. Figure 6c is based on grids in which observations of both

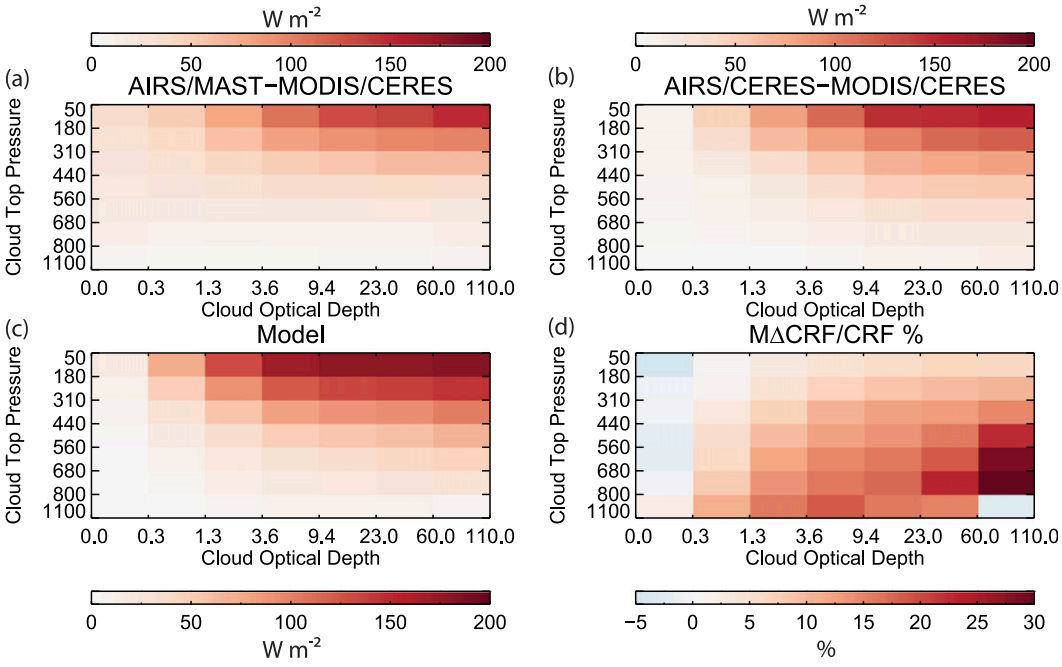

FIG. 5. The CRF by cloud type after removing the MΔCRF for (a) the AIRS–MAST-MODIS–CERES data, (b) the AIRS–CERES-MODIS–CERES data, and (c) the calculated CRF by the Fu–Liou model. The MERRA atmospheric state that is collocated to the satellite observations, the mean cloud properties from the MODIS-MAST cloud retrieval, and the monthly mean vertical distribution of τ obtained from *CloudSat* 2B-TAU data are used as input to the Fu–Liou model for (c). (d) The contribution of the MΔCRF as a percentage of the total CRF by cloud type.

clear and cloudy skies are available during July 2009. This sampling is not applied to CRKs shown in Fig. 6d, as latitudinal mean atmospheric profiles and synthetic clouds are used. Another difference is the 1330 LT orbital sampling of the A-Train. These differences described above may contribute to differences between the two sets of CRKs using radiative transfer calculations. Although the sampling provided by the A-Train limits the diurnal coverage and leads to difficulties in obtaining global coverage, a more realistic geophysical distribution of clouds and TOA radiative sensitivity to cloud type is obtained.

Despite differences in methodology, sampling, and data sources, it is clear in Fig. 6 that all four sets of longwave CRKs show a similar dependence on cloud type. Compared with CRKs in Zhou et al. (2013), the observation-based CRKs generally show larger magnitudes for low cloud and optically thin cloud. For deep and optically thick clouds, a very good agreement between observation-based CRKs and CRKs in Zhou et al. (2013) is found since the CTP given by the CO_2-slicing method is quite close to the radiative effective cloud top.

d. Uncertainties in deriving CRKs

In this section, we discuss the uncertainties from the calculation of longwave CRKs caused by the atmospheric contribution MΔCRF [Eq. (5)], different definitions of clear sky, two MODIS cloud retrieval algorithms, and the assumption of a single-layer cloud.

As discussed previously, MΔCRF contributes within 10% to the total OLR but is as large as 28% of the total CRF for optically thick clouds at low and middle levels. The contribution to the CRK is calculated as ∂MΔCRF/∂C [Eq. (6)] and is shown in Fig. 7. While the largest absolute contribution is within optically thick high cloud ($0.1\,\mathrm{W\,m^{-2}\ \%^{-1}}$), the MΔCRF accounts for 10%–30% of the CRK for low and midlevel optically thick clouds. Therefore, the cloud radiative effect from the cloud's impact on atmospheric states should not be neglected when calculating CRF and observation-based CRKs but can be estimated from clear-sky TOA radiative fluxes from reanalysis that are matched to cloud observations or using the method in this study. Figure 7 also suggests a possible range of uncertainties in the longwave CRK that is caused by variations of MΔCRF.

The differences caused by the two types of MODIS retrieval algorithms are shown in Fig. 8. From Eqs. (4) and (6), the observation-based CRKs depend on both CRF and CF stratified by CTP–τ bins. Since the cloud retrievals from two different algorithms are constrained by the same TOA radiation, the differences in the cloud properties themselves compensate with the differences

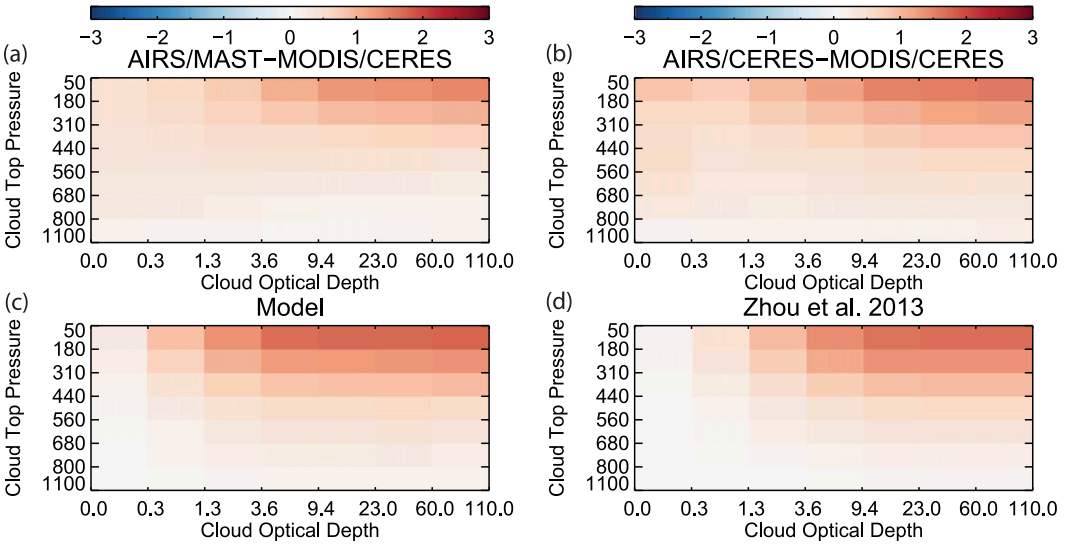

FIG. 6. CRKs ($W\,m^{-2}\,\%^{-1}$) obtained by different data and methods. (a) Observation-based CRK using the AIRS–MAST-MODIS–CERES data. (b) Observation-based CRK using the AIRS–CERES-MODIS–CERES data. (c) Model-based CRK calculated using the Fu–Liou model with collocated MERRA and satellite data as additional input. (d) CRK for July as described in Zhou et al. (2013).

in CRF calculations. As a result, the observation-based CRK in general has a smaller dependence on the MODIS retrieval algorithm than CRF and CF by cloud type. On the other hand, this again emphasizes the importance of maintaining consistency between the TOA radiative sensitivity as demonstrated by CRKs and observed cloud changes when estimating cloud feedbacks from remote sensing data. However, the uncertainties of the observation-based CRKs caused by MODIS missing optically thin clouds and assigning cloud top at the wrong altitude persist.

The absolute and relative differences of clear-sky thresholds on CRK are shown in Figs. 9a–d and are small: less than $\pm 0.05\,W\,m^{-2}\,\%^{-1}$ (20%) for CRK (less than $\pm 3\,W\,m^{-2}$ for CRF). A more conservative clear-sky threshold such as Clear-2 slightly increases the magnitude of the longwave CRK, especially for optically thin cloud and low cloud. Thus, if perfect clear conditions are available, the magnitude of CRKs for optically thin cloud and low cloud may be larger than using Clear-2. Slight changes with Clear-3 are also noted.

To test the impact of a single-layer assumption, we obtain the cloud vertical distribution by using the monthly mean profiles of τ from the *CloudSat* 2B-TAU product. The mean vertical τ profile is generated for each bin on the CTP–τ histogram. Low-cloud types with CTP $>$ 800 hPa are excluded because of high uncertainties of *CloudSat*-detected cloud near the surface (Tanelli et al. 2008); bins with $\tau < 0.3$ are also excluded because of high uncertainties in both MODIS and *CloudSat* data. The effective radius is assumed to be vertically uniform and the cloud is further assumed to be horizontally uniform for the Fu–Liou calculation. The impact of cloud vertical structure on the longwave CRK is quantified by comparing the Fu–Liou calculations using a single-layer assumption and results using the mean τ profiles by cloud type, and the results are shown in Figs. 9e and 9f. The inclusion of the τ vertical distribution increases the magnitude of CRKs for high cloud, while it decreases for midlevel cloud. The relative difference is between −10% and +12% depending on the cloud type.

The standard deviation of observation-based CRKs among grid boxes is shown in Fig. 10. Both the MAST-MODIS- and CERES-MODIS-based CRKs show large variances over land for $\tau < 9.6$. For CERES-MODIS CRKs, large variances are found for optically thinnest cloud both over land and ocean. (These patterns remain the same even if the sample size is increased to an entire year's worth of observations.) For MAST-MODIS CRKs, there is little or no variance over the ocean across all of the cloud types and also over land for $\tau > 9.6$. Since similar diurnal and orbital sampling is applied over land and ocean, it is unlikely that the ocean–land differences are due to these sampling biases. Moreover, the variance for optically thinner cloud is much larger over desert and high-latitude regions than other land types (not shown). Therefore, this large variance may be partially caused by higher uncertainties in optically thin cloud properties and also for calculations or observations of radiative fluxes over land.

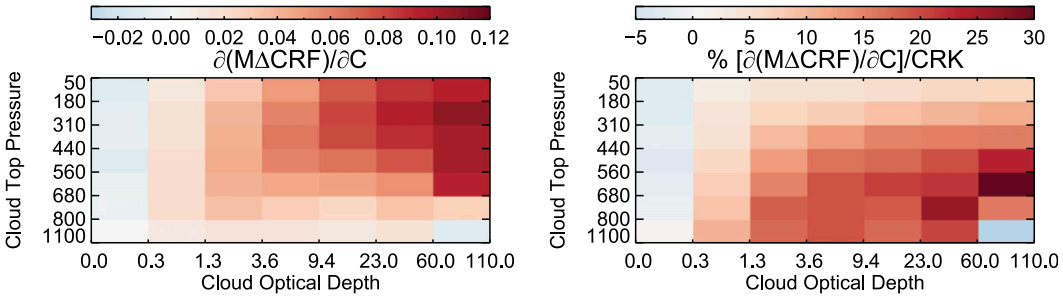

FIG. 7. (left) The contribution of MΔCRF to CRK (∂MΔCRF/∂C; W m^{-2} %$^{-1}$) in Eq. (6) and (right) the contribution as a percentage of the observation-based CRK.

Moreover, the results presented in this study are based on one month of collocated satellite measurements to describe the methodology and uncertainty analysis. We also tested this method by limiting the analysis to 15 days of observations, and similar results are obtained for most cloud types except for the optically thinnest clouds at all CTP bins and low clouds, with CTP > 800 hPa at the largest optical depth bin in the MAST-MODIS data (not shown).

e. *The AIRS spectral cloud radiative effects*

The frequency dependence of OLR and longwave CRF is important to better understand the connection

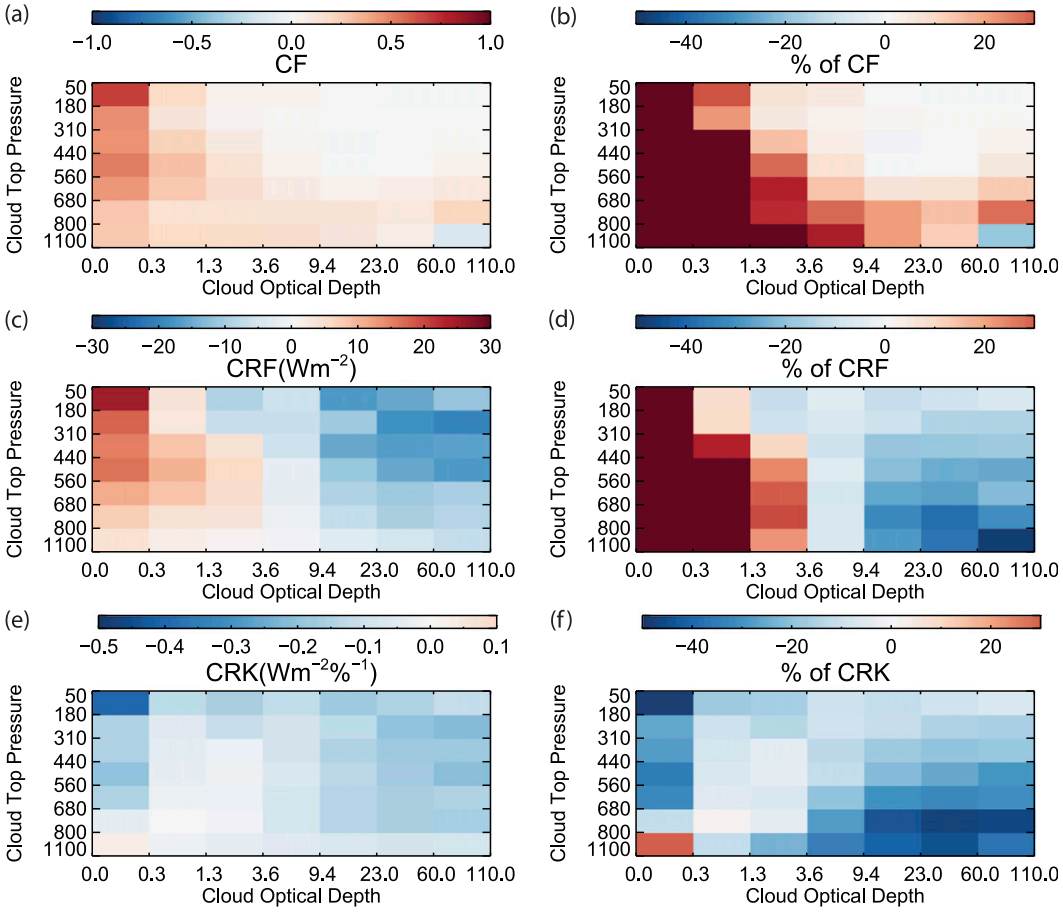

FIG. 8. Differences in (a),(b) CF, (c),(d) CRF, and (e),(f) CRK between results using AIRS–MAST-MODIS–CERES data and those using AIRS–CERES-MODIS–CERES data. In (a),(c),(e) the differences in CF (0–1, no units), CRF (W m^{-2}), and CRK (W m^{-2} %$^{-1}$), respectively. In (b),(d),(f) the differences in percentage relative to AIRS–CERES-MODIS–CERES for CF, CRF, and CRK, respectively. The same color bar is used for (b),(d),(f) to emphasize the CRK. The maximum magnitudes for CF and CRF are well above 100%.

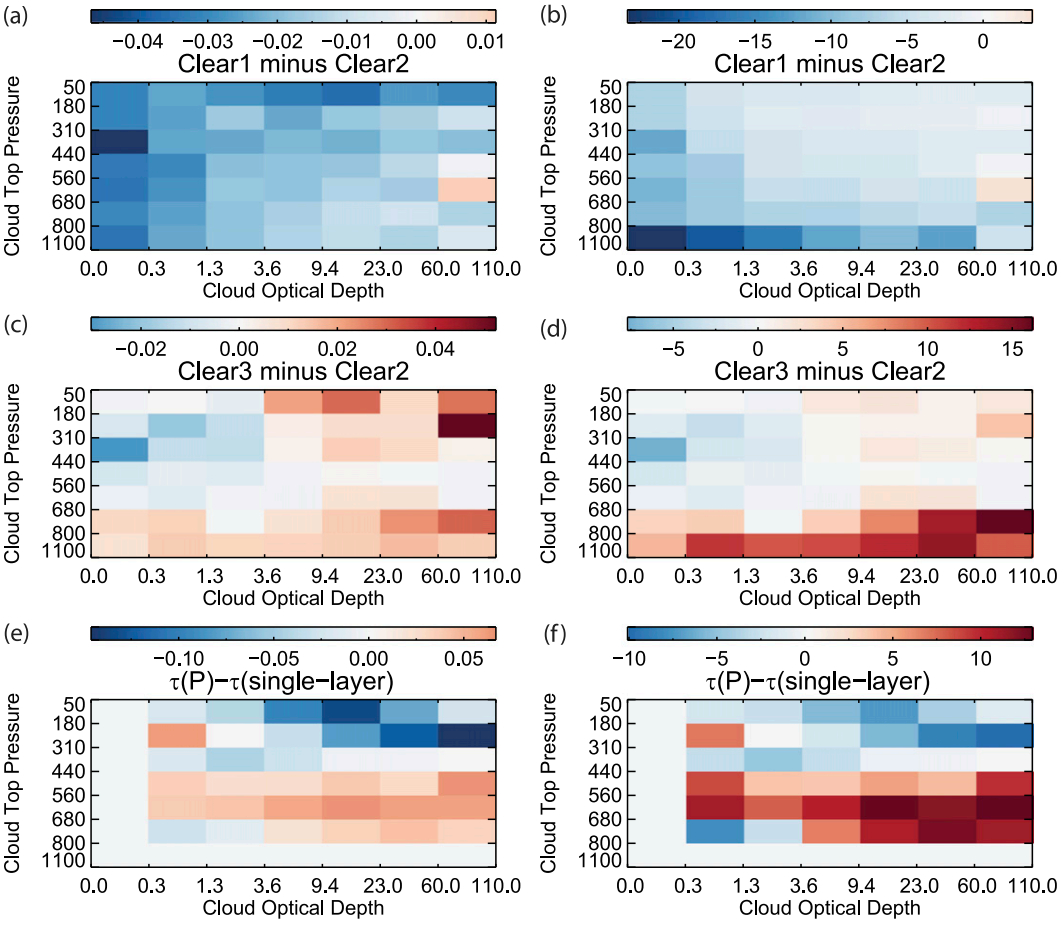

FIG. 9. Uncertainties due to (a)–(d) clear-sky thresholds and (e),(f) vertical distribution of τ (multiple-layer cloud minus single-layer cloud). (left) Absolute difference on CRK ($\mathrm{W\,m^{-2}\,\%^{-1}}$) and (right) relative difference (%) of AIRS–MAST-MODIS–CERES CRK in (b) and (d) and model-based CRKs calculated in this study in (f).

between band-by-band fluxes, cloud properties, and atmospheric states (Huang et al. 2014a). The AIRS spectral OLR dataset developed with collocated CERES broadband measurements (Huang et al. 2008, 2010, 2013) is used to demonstrate that a frequency-dependent spectral longwave CRK can be derived and evaluated.

The entire infrared spectrum is subdivided into the far infrared (FIR; $<715\,\mathrm{cm^{-1}}$ or $>14\,\mu$m) and midinfrared (MIR; 833–2000 $\mathrm{cm^{-1}}$ or 5–12 μm). The spectral OLR and CRF have similar dependences on cloud type with the total OLR (not shown). Note that the spectral CRF and CRK do not have an equivalent ΔCRF effect removed since the cloud-type-dependent spectral F_{clr}[cloud. removed] data are not available at the time of this study. The applicability of our method is demonstrated with spectrally resolved OLR data.

The observation-based, cloud-type-dependent spectral CRK shows a strong spectral dependence. Figure 11 shows the oceanic MIR and FIR spectral CRK. The FIR/MIR ratio varies between 0.1 and 0.6, with larger values for thin and high clouds and smaller values for low clouds. As clouds lower, the cloud-top temperature increases and thus the peak of the Planck function shifts toward shorter wavelengths, consistent with this behavior. The FIR effect increases for optically thin clouds, where the cloud radiative effects are small and compete with the atmospheric radiative effects.

4. Summary

We investigate cloud radiative effects and present a new method to derive an observation-based cloud radiative kernel (CRK). A global gridded dataset of atmospheric temperature and moisture, cloud properties, and TOA spectral and broadband radiative fluxes is constructed for a range of cloud types starting with pixel-scale collocated, multisensor observations from the NASA A-Train satellite constellation and MERRA data. Cloud type is defined using the classification of

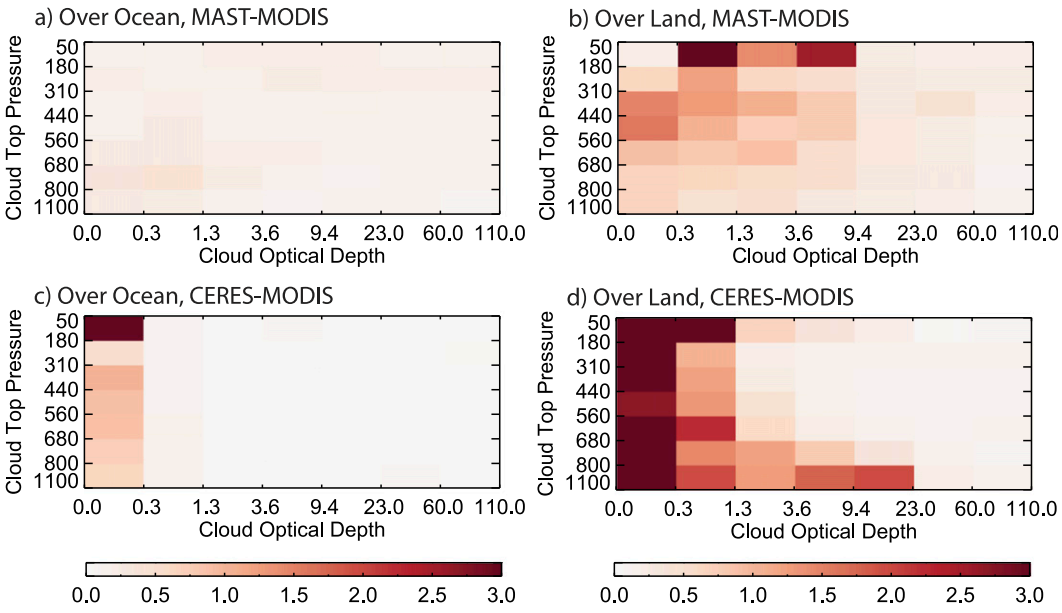

FIG. 10. Standard deviation of observation-based CRKs ($W\,m^{-2}\,\%^{-1}$) from grid boxes over (a),(c) ocean and (b), (d) land based on MAST-MODIS cloud retrievals in (a) and (b) and CERES-MODIS cloud retrievals in (c) and (d).

International Satellite Cloud Climatology Project (ISCCP) and is partitioned into seven cloud-top pressure (CTP) bins and seven cloud optical depth τ bins. Using AIRS effective cloud fraction (ECF) and MODIS cloud fraction (CF) data, we investigate three clear-sky definitions using different thresholds of cloud amount for a given satellite pixel. Within each grid box and cloud type, the monthly mean values of CERES broadband outgoing longwave radiation (OLR), AIRS–CERES spectral OLR, MODIS cloud properties from the CERES science team (CERES-MODIS) and the MODIS atmosphere science team (MAST-MODIS), and atmospheric states from MERRA data are determined.

There are two components of the observationally derived TOA cloud radiative effect. One is the radiative effect solely from cloud properties such as CTP and cloud-top temperature (CTT), CF, τ, and cloud effective radius r_e. The other is the radiative effect solely from differences of atmospheric temperature and moisture profiles between clear and cloudy skies (ΔCRF). Both components are quantified as a function of cloud type using a combination of observations and clear-sky calculations using the Fu and Liou (1992) radiative transfer model. We find that ΔCRF contributes only up to 10% of the total OLR and is largest for optically thick high clouds. However, its contributions to longwave cloud radiative forcing (CRF) and CRK are up to 30% for optically thick low clouds and 10% for optically thick high clouds. Because of the differences in atmospheric states between clear and cloudy skies, a proper comparison to model-derived CRFs and CRKs requires the removal of ΔCRF from the observationally derived values.

Although forward radiative transfer and assumptions on cloud, atmosphere, and radiation are intrinsic to satellite remote sensing, these observations have been extensively validated and algorithms have been optimized to provide high-quality, near-real-time measurements that are representative of nature. The observation-based CRK method directly makes use of readily available satellite measurements. Furthermore, there is no need to carry out additional cloudy-sky radiative transfer and assume cloud properties that are not inherently consistent with the observations. Since the CRKs presented in this work are empirically derived from TOA flux and cloud observations, they indicate the TOA radiative sensitivity of particular cloud types that are observed by EOS *Aqua* instruments. Therefore, a combination of such CRKs with cloud changes observed by these instruments over time will provide an estimate of the short-term cloud feedback by maintaining consistency between CRKs and cloud responses to climate variability.

We also derive a set of cloud-type-dependent model-based CRKs using the Fu–Liou model code following the approach of Zelinka et al. (2012) and Zhou et al. (2013) but using collocated atmospheric and cloud data from MERRA and MODIS. The observation- and model-based CRKs show very similar patterns of cloud-type dependence especially for optically thick and high clouds. Some differences are seen for optically thin clouds; that is, the observation-based CRKs have a

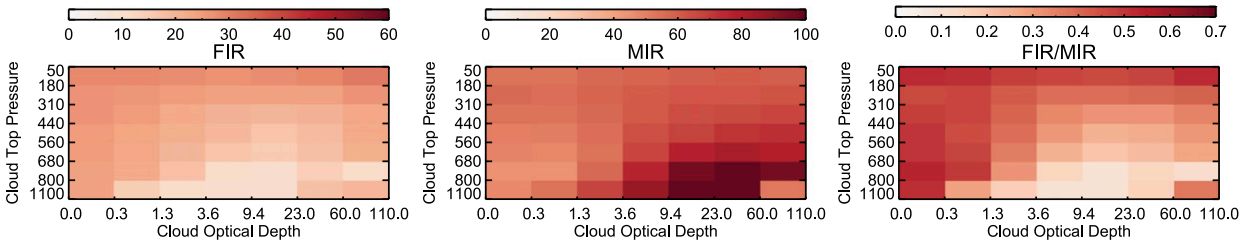

FIG. 11. Percentage of AIRS spectral CRK by cloud type contributed from two separate infrared spectral regions: (left) FIR (>14 μm) and (center) MIR (5–12 μm). (right) The ratio between the FIR and MIR.

larger TOA radiative sensitivity than the model-derived ones. From sensitivity tests on clear-sky thresholds, the observation-based CRK values may further increase, especially for optically thin clouds. However, the uncertainty of observation-based CRKs for thin cloud is larger because MODIS underestimates the detection of optically thin cloud (Holz et al. 2008; Ackerman et al. 2008). We further evaluate the uncertainties of longwave CRKs from the assumption of a single cloud layer. We difference radiative transfer calculations with and without mean vertical profiles of τ for each cloud type using the *CloudSat* 2B-TAU product. By including the τ profiles, the model-based CRK values are decreased for high cloud and increased for middle and low clouds; however, the relative contribution is generally within $\pm$10%.

We find that the retrieval method uncertainty inferred from the two types of MODIS retrievals is very large for cloud-type-dependent CF and CRF (see Fig. 8) but is much smaller for CRKs within cloud types with $\tau < 3.6$. We speculate that differences in the cloud properties compensate in the CRK calculations since both MODIS retrieval methods require consistency with observed outgoing radiances. However, the sensitivity of the observation-based CRKs to the retrieval methods is not negligible, which suggests the importance of consistency between CRKs and cloud fraction changes to estimate short-term cloud feedback from remote sensing data.

The new observation-based CRK method makes use of a number of collocated A-Train satellite measurements. It is independent of climate simulations on either cloud or atmosphere. This method does not require additional cloudy-sky radiative transfer calculations with assumptions about cloud radiative, microphysical, and macrophysical properties. The removal of atmospheric contributions is achieved by clear-sky radiative transfer calculations. While the sampling provided by the A-Train is limited and cannot obtain global coverage across the full diurnal cycle for all cloud types, it does provide a more realistic radiative sensitivity of TOA radiative fluxes to cloud types observed by MODIS instruments. The CRKs developed based on the method in this study can be used to estimate cloud feedbacks from changes in MODIS cloud properties and perhaps from other cloud imagers such as the Advanced Very High Resolution Radiometer and visible infrared imaging radiometer suite.

Acknowledgments. The research described in this paper was carried out at the Jet Propulsion Laboratory, California Institute of Technology, under a contract with the National Aeronautics and Space Administration. QY, BHK, EJF, MS, and SW were supported by NASA's Making Earth Science Data Records for Use in Research Environments (MEaSUREs) program. QY, EJF, MS, SW, and BHK acknowledge the support of the AIRS project at JPL. The efforts of X. L. Huang and X. H. Chen were supported by NASA Grant NNX14AJ50G awarded to the University of Michigan. AIRS data were obtained through the Goddard Earth Services Data and Information Services Center (http://daac.gsfc.nasa.gov/). MODIS data were obtained through the Level-1 and Atmosphere Archive and Distribution System (LAADS; http://ladsweb.nascom.nasa.gov/). The authors thank B. Soden, M. Zelinka, and G. Stephens for useful feedback in the preparation of this manuscript and the anonymous reviewers for comments on this study.

REFERENCES

Ackerman, S. A., R. E. Holz, R. Frey, E. W. Eloranta, B. C. Maddux, and M. McGill, 2008: Cloud detection with MODIS. Part II: Validation. *J. Atmos. Oceanic Technol.*, **25**, 1073–1086, doi:10.1175/2007JTECHA1053.1.

Aumann, H. H., and Coauthors, 2003: AIRS/AMSU/HSB on the Aqua mission: Design, science objectives, data products, and processing system. *IEEE Trans. Geosci. Remote Sens.*, **41**, 253–264, doi:10.1109/TGRS.2002.808356.

Barnes, W. L., T. S. Pagano, and V. V. Salomonson, 1998: Prelaunch characteristics of the Moderate Resolution Imaging Spectroradiometer (MODIS) on EOS-AM1. *IEEE Trans. Geosci. Remote Sens.*, **36**, 1088–1100, doi:10.1109/36.700993.

Bony, S., and Coauthors, 2006: How well do we understand and evaluate climate change feedback processes? *J. Climate*, **19**, 3445–3482, doi:10.1175/JCLI3819.1.

Chahine, M. T., 1974: Remote sounding of cloudy atmospheres. I. The single cloud layer. *J. Atmos. Sci.*, **31**, 233–243, doi:10.1175/1520-0469(1974)031<0233:RSOCAI>2.0.CO;2.

Charlock, T. P., and V. Ramanathan, 1985: The albedo field and cloud radiative forcing produced by a general circulation model with internally generated cloud optics. *J. Atmos. Sci.*, **42**, 1408–1429, doi:10.1175/1520-0469(1985)042<1408:TAFACR>2.0.CO;2.

Chen, X., X. L. Huang, N. G. Loeb, and H. Wei, 2013: Comparisons of clear-sky outgoing far-IR flux inferred from satellite observations and computed from the three most recent reanalysis products. *J. Climate*, **26**, 478–494, doi:10.1175/JCLI-D-12-00212.1.

Dessler, A. E., 2010: A determination of the cloud feedback from climate variations over the past decade. *Science*, **330**, 1523–1527, doi:10.1126/science.1192546.

——, and N. G. Loeb, 2013: Impact of dataset choice on calculations of the short-term cloud feedback. *J. Geophys. Res.*, **118**, 2821–2826, doi:10.1002/jgrd.50199.

Dufresne, J.-L., and S. Bony, 2008: An assessment of the primary sources of spread of global warming estimates from coupled atmosphere–ocean models. *J. Climate*, **21**, 5135–5144, doi:10.1175/2008JCLI2239.1.

Fu, Q., and K. N. Liou, 1992: On the correlated *k*-distribution method for radiative transfer in nonhomogeneous atmospheres. *J. Atmos. Sci.*, **49**, 2139–2156, doi:10.1175/1520-0469(1992)049<2139:OTCDMF>2.0.CO;2.

Gregory, J. M., R. J. Stouffer, S. C. B. Raper, P. A. Stott, and N. A. Rayner, 2002: An observationally based estimate of the climate sensitivity. *J. Climate*, **15**, 3117–3121, doi:10.1175/1520-0442(2002)015<3117:AOBEOT>2.0.CO;2.

Hartmann, D. L., M. E. Ockert-Bell, and M. L. Michelsen, 1992: The effect of cloud type on Earth's energy balance: Global analysis. *J. Climate*, **5**, 1281–1304, doi:10.1175/1520-0442(1992)005<1281:TEOCTO>2.0.CO;2.

Held, I. M., and B. J. Soden, 2000: Water vapor feedback and global warming. *Annu. Rev. Energy Environ.*, **25**, 441–475, doi:10.1146/annurev.energy.25.1.441.

Holz, R. E., S. A. Ackerman, F. W. Nagle, R. Frey, S. Dutcher, R. E. Kuehn, M. A. Vaughan, and B. Baum, 2008: Global Moderate Resolution Imaging Spectroradiometer (MODIS) cloud detection and height evaluation using CALIOP. *J. Geophys. Res.*, **113**, D00A19, doi:10.1029/2008JD009837.

Huang, X. L., W. Z. Yang, N. G. Loeb, and V. Ramaswamy, 2008: Spectrally resolved fluxes derived from collocated AIRS and CERES measurements and their application in model evaluation: 1. Clear sky over the tropical oceans. *J. Geophys. Res.*, **113**, D09110, doi:10.1029/2007JD009219.

——, N. G. Loeb, and W. Z. Yang, 2010: Spectrally resolved fluxes derived from collocated AIRS and CERES measurements and their application in model evaluation: 2. Cloudy sky and band-by-band cloud radiative forcing over the tropical oceans. *J. Geophys. Res.*, **115**, D21101, doi:10.1029/2010JD013932.

——, J. N. S. Cole, F. He, G. L. Potter, L. Oreopoulos, D. M. Lee, M. Suarez, and N. G. Loeb, 2013: Longwave band-by-band cloud radiative effect and its application in GCM evaluation. *J. Climate*, **26**, 450–467, doi:10.1175/JCLI-D-12-00112.1.

——, X. Chen, G. L. Potter, L. Oreopoulos, J. N. S. Cole, D. Lee, and N. G. Loeb, 2014a: A global climatology of outgoing longwave spectral cloud radiative effect and associated effective cloud properties. *J. Climate*, **27**, 7475–7492, doi:10.1175/JCLI-D-13-00663.1.

——, ——, B. J. Soden, and X. Liu, 2014b: The spectral dimension of longwave feedback in the CMIP3 and CMIP5 experiments. *Geophys. Res. Lett.*, **41**, 7830–7837, doi:10.1002/2014GL061938.

IPCC, 2013: *Climate Change 2013: The Physical Science Basis*. Cambridge University Press, 1535 pp., doi:10.1017/CBO9781107415324.

Kahn, B. H., and Coauthors, 2014: The Atmospheric Infrared Sounder version 6 cloud products. *Atmos. Chem. Phys.*, **14**, 399–426, doi:10.5194/acp-14-399-2014.

Klein, S. A., and C. Jakob, 1999: Validation and sensitivities of frontal clouds simulated by the ECMWF model. *Mon. Wea. Rev.*, **127**, 2514–2531, doi:10.1175/1520-0493(1999)127<2514:VASOFC>2.0.CO;2.

Lambert, F. H., M. J. Webb, M. Yoshimori, and T. Yokohata, 2014: The cloud radiative effect on the atmospheric energy budget and global mean precipitation. *Climate Dyn.*, **44**, 2301–2325, doi:10.1007/s00382-014-2174-9.

Lambrigtsen, B. H., and S.-Y. Lee, 2003: Coalignment and synchronization of the AIRS instrument suite. *IEEE Trans. Geosci. Remote Sens.*, **41**, 343–351, doi:10.1109/TGRS.2002.808246.

Loeb, N. G., S. Kato, K. Loukachine, N. Manalo-Smith, and D. R. Doelling, 2005: Angular distribution models for top-of-atmosphere radiative flux estimation from the Clouds and the Earth's Radiant Energy System instrument on the *Terra* satellite. Part I: Methodology. *J. Atmos. Oceanic Technol.*, **22**, 338–351, doi:10.1175/JTECH1712.1.

Marchand, R., 2013: Trends in ISCCP, MISR, and MODIS cloud-top-height and optical-depth histograms. *J. Geophys. Res.*, **118**, 1941–1949, doi:10.1002/jgrd.50207.

Minnis, P., and Coauthors, 2011a: CERES edition-2 cloud property retrievals using TRMM VIRS and *Terra* and *Aqua* MODIS data—Part I: Algorithms. *IEEE Trans. Geosci. Remote Sens.*, **49**, 4374–4400, doi:10.1109/TGRS.2011.2144601.

——, and Coauthors, 2011b: CERES edition-2 cloud property retrievals using TRMM VIRS and *Terra* and *Aqua* MODIS data—Part II: Examples of average results and comparisons with other data. *IEEE Trans. Geosci. Remote Sens.*, **49**, 4401–4430, doi:10.1109/TGRS.2011.2144602.

Nasiri, S. L., H. V. T. Dang, B. H. Kahn, E. J. Fetzer, E. M. Manning, M. M. Schreier, and R. A. Frey, 2011: Comparing MODIS and AIRS infrared-based cloud retrievals. *J. Appl. Meteor. Climatol.*, **50**, 1057–1072, doi:10.1175/2010JAMC2603.1.

Parkinson, C. L., 2003: *Aqua*: An Earth-observing satellite mission to examine water and other climate variables. *IEEE Trans. Geosci. Remote Sens.*, **41**, 173–183, doi:10.1109/TGRS.2002.808319.

Pincus, R., S. Platnick, S. A. Ackerman, R. S. Hemler, and R. J. P. Hofmann, 2012: Reconciling simulated and observed views of clouds: MODIS, ISCCP, and the limits of instrument simulators. *J. Climate*, **25**, 4699–4720, doi:10.1175/JCLI-D-11-00267.1.

Platnick, S., M. D. King, S. A. Ackerman, W. P. Menzel, B. A. Baum, J. C. Riédi, and R. A. Frey, 2003: The MODIS cloud products: Algorithms and examples from *Terra*. *IEEE Trans. Geosci. Remote Sens.*, **41**, 459–473, doi:10.1109/TGRS.2002.808301.

Ramanathan, V., R. D. Cess, E. F. Harrison, P. Minnis, B. R. Barkstrom, E. Ahmad, and D. Hartmann, 1989: Cloud-radiative forcing and climate: Results from the Earth Radiation Budget Experiment. *Science*, **243**, 57–63, doi:10.1126/science.243.4887.57.

Rienecker, M. M., and Coauthors, 2011: MERRA: NASA's Modern-Era Retrospective Analysis for Research and Applications. *J. Climate*, **24**, 3624–3648, doi:10.1175/JCLI-D-11-00015.1.

Rossow, W. B., and R. A. Schiffer, 1999: Advances in understanding clouds from ISCCP. *Bull. Amer. Meteor. Soc.*, **80**, 2261–2287, doi:10.1175/1520-0477(1999)080<2261:AIUCFI>2.0.CO;2.

Sanderson, B. M., and K. M. Shell, 2012: Model-specific radiative kernels for calculating cloud and noncloud climate feedbacks. *J. Climate*, **25**, 7607–7624, doi:10.1175/JCLI-D-11-00726.1.

Schreier, M. M., B. H. Kahn, A. Eldering, D. A. Elliott, E. Fishbein, F. W. Irion, and T. S. Pagano, 2010: Radiance comparisons of MODIS and AIRS using spatial response information. *J. Atmos. Oceanic Technol.*, **27**, 1331–1342, doi:10.1175/2010JTECHA1424.1.

Shell, K. M., J. T. Kiehl, and C. A. Shields, 2008: Using the radiative kernel technique to calculate climate feedbacks in NCAR's Community Atmospheric Model. *J. Climate*, **21**, 2269–2282, doi:10.1175/2007JCLI2044.1.

Soden, B. J., and I. M. Held, 2006: An assessment of climate feedbacks in coupled ocean–atmosphere models. *J. Climate*, **19**, 3354–3360, doi:10.1175/JCLI3799.1.

——, A. J. Broccoli, and R. S. Hemler, 2004: On the use of cloud forcing to estimate cloud feedback. *J. Climate*, **17**, 3661–3665, doi:10.1175/1520-0442(2004)017<3661:OTUOCF>2.0.CO;2.

——, I. M. Held, R. Colman, K. M. Shell, J. T. Kiehl, and C. A. Shields, 2008: Quantifying climate feedbacks using radiative kernels. *J. Climate*, **21**, 3504–3520, doi:10.1175/2007JCLI2110.1.

Stephens, G. L., 2005: Cloud feedbacks in the climate system: A critical review. *J. Climate*, **18**, 237–273, doi:10.1175/JCLI-3243.1.

——, and Coauthors, 2002: The *CloudSat* mission and the A-Train: A new dimension of space-based observations of clouds and precipitation. *Bull. Amer. Meteor. Soc.*, **83**, 1771–1790, doi:10.1175/BAMS-83-12-1771.

Suarez, M. J., and Coauthors, 2008: The GEOS-5 data assimilation system—Documentation of versions 5.0.1, 5.1.0, and 5.2.0. NASA Tech. Memo. NASA/TM-2008-104606, 97 pp.

Tanelli, S., S. L. Durden, E. Im, K. S. Pak, D. Reinke, P. Partain, R. Marchand, and J. Haynes, 2008: *CloudSat's* cloud profiling radar after two years in orbit: Performance, calibration, and processing. *IEEE Trans. Geosci. Remote Sens.*, **46**, 3560–3573, doi:10.1109/TGRS.2008.2002030.

Vial, J., J.-L. Dufresne, and S. Bony, 2013: On the interpretation of inter-model spread in CMIP5 climate sensitivity estimates. *Climate Dyn.*, **41**, 3339–3362, doi:10.1007/s00382-013-1725-9.

Webb, M., C. Senior, S. Bony, and J. J. Morcrette, 2001: Combining ERBE and ISCCP data to assess clouds in the Hadley Centre, ECMWF and LMD atmospheric climate models. *Climate Dyn.*, **17**, 905–922, doi:10.1007/s003820100157.

——, and Coauthors, 2006: On the contribution of local feedback mechanisms to the range of climate sensitivity in two GCM ensembles. *Climate Dyn.*, **27**, 17–38, doi:10.1007/s00382-006-0111-2.

Wielicki, B. A., B. R. Barkstrom, E. F. Harrison, R. B. Lee III, G. Louis Smith, and J. E. Cooper, 1996: Clouds and the Earth's Radiant Energy System (CERES): An Earth observing system experiment. *Bull. Amer. Meteor. Soc.*, **77**, 853–868, doi:10.1175/1520-0477(1996)077<0853:CATERE>2.0.CO;2.

Williams, K. D., and G. Tselioudis, 2007: GCM intercomparison of global cloud regimes: Present-day evaluation and climate change response. *Climate Dyn.*, **29**, 231–250, doi:10.1007/s00382-007-0232-2.

——, and M. J. Webb, 2009: A quantitative performance assessment of cloud regimes in climate models. *Climate Dyn.*, **33**, 141–157, doi:10.1007/s00382-008-0443-1.

Wong, S., E. J. Fetzer, M. Schreier, G. Manipon, E. F. Fishbein, B. H. Kahn, Q. Yue, and F. W. Irion, 2015: Cloud-induced uncertainties in AIRS and ECMWF temperature and specific humidity. *J. Geophys. Res. Atmos.*, **120**, 1880–1901, doi:10.1002/2014JD022440.

Yue, Q., K. N. Liou, S. C. Ou, B. H. Kahn, P. Yang, and G. G. Mace, 2007: Interpretation of AIRS data in thin cirrus atmospheres based on a fast radiative transfer model. *J. Atmos. Sci.*, **64**, 3827–3842, doi:10.1175/2007JAS2043.1.

——, E. J. Fetzer, B. H. Kahn, S. Wong, G. Manipon, A. Guilaume, and B. Wilson, 2013: Cloud-state-dependent sampling in AIRS observations based on *CloudSat* cloud classification. *J. Climate*, **26**, 8357–8377, doi:10.1175/JCLI-D-13-00065.1.

Zelinka, M. D., S. A. Klein, and D. L. Hartmann, 2012: Computing and partitioning cloud feedbacks using cloud property histograms. Part I: Cloud radiative kernels. *J. Climate*, **25**, 3715–3735, doi:10.1175/JCLI-D-11-00248.1.

Zhang, M. H., R. D. Cess, T. Y. Kwon, and M. H. Chen, 1994a: Approaches of comparison for clear-sky radiative fluxes from general circulation models with Earth Radiation Budget Experiment data. *J. Geophys. Res.*, **99**, 5515–5523, doi:10.1029/93JD03341.

——, J. J. Hack, J. T. Kiehl, and R. D. Cess, 1994b: Diagnostic study of climate feedback processes in atmospheric general circulation models. *J. Geophys. Res.*, **99**, 5525–5537, doi:10.1029/93JD03523.

Zhou, C., M. D. Zelinka, A. E. Dessler, and P. Yang, 2013: An analysis of the short-term cloud feedback using MODIS data. *J. Climate*, **26**, 4803–4815, doi:10.1175/JCLI-D-12-00547.1.